

Properties of air mass mixing and humidity in the subtropics from measurements of the D/H isotope ratio of water vapor at the Mauna Loa Observatory

David Noone,^{1,2} Joseph Galewsky,³ Zachary D. Sharp,³ John Worden,⁴ John Barnes,⁵ Doug Baer,⁶ Adriana Bailey,^{1,2} Derek P. Brown,^{1,2} Lance Christensen,⁴ Eric Crosson,⁷ Feng Dong,⁶ John V. Hurley,³ Leah R. Johnson,³ Mel Strong,³ Darin Toohey,¹ Aaron Van Pelt,⁷ and Jonathon S. Wright⁸

Received 3 February 2011; revised 7 September 2011; accepted 9 September 2011; published 23 November 2011.

[1] Water vapor in the subtropical troposphere plays an important role in the radiative balance, the distribution of precipitation, and the chemistry of the Earth's atmosphere. Measurements of the water vapor mixing ratio paired with stable isotope ratios provide unique information on transport processes and moisture sources that is not available with mixing ratio data alone. Measurements of the D/H isotope ratio of water vapor from Mauna Loa Observatory over 4 weeks in October–November 2008 were used to identify components of the regional hydrological cycle. A mixing model exploits the isotope information to identify water fluxes from time series data. Mixing is associated with exchange between marine boundary layer air and tropospheric air on diurnal time scales and between different tropospheric air masses with characteristics that evolve on the synoptic time scale. Diurnal variations are associated with upslope flow and the transition from nighttime air above the marine trade inversion to marine boundary layer air during daytime. During easterly trade wind conditions, growth and decay of the boundary layer are largely conservative in a regional context but contribute ~12% of the nighttime water vapor at Mauna Loa. Tropospheric moisture is associated with convective outflow and exchange with drier air originating from higher latitude or higher altitude. During the passage of a moist filament, boundary layer exchange is enhanced. Isotopic data reflect the combination of processes that control the water balance, which highlights the utility for baseline measurements of water vapor isotopologues in monitoring the response of the hydrological cycle to climate change.

Citation: Noone, D., et al. (2011), Properties of air mass mixing and humidity in the subtropics from measurements of the D/H isotope ratio of water vapor at the Mauna Loa Observatory, *J. Geophys. Res.*, 116, D22113, doi:10.1029/2011JD015773.

1. Introduction

[2] Water vapor and clouds are important for radiative balance and the distribution of precipitation. Their influence largely determines the strength of the greenhouse

effect [Arrhenius, 1896; Manabe and Wetherald, 1975; Pierrehumbert, 1995] and the sensitivity of the climate system response to anthropogenic forcings [Bony et al., 2006; Held and Soden, 2006; Schmidt et al., 2010]. The atmospheric water cycle can be conceptualized as the balance between sources at the earth surface, sinks associated with condensation and transport processes associated with moist convection, turbulence, and large-scale atmospheric motion [Schneider et al., 2010b; Sherwood et al., 2010]. Understanding the processes that control the subtropical water budget is of particular importance because of the disproportionate role subtropical water vapor plays in determining the Earth's radiative balance and because of anticipated changes to the subtropics with climate change [Seidel et al., 2008]. The isotopic composition of water captures the history of phase changes [Jouzel, 1986; Gat, 2000], and therefore measurements of the hydrogen isotope ratios in water vapor can be used to help identify the frequency and prevalence of the water vapor fluxes at daily and synoptic time scales.

¹Department of Atmospheric and Oceanic Sciences, University of Colorado at Boulder, Boulder, Colorado, USA.

²Cooperative Institute for Research in Environmental Sciences, University of Colorado at Boulder, Boulder, Colorado, USA.

³Department of Earth and Planetary Sciences, University of New Mexico, Albuquerque, New Mexico, USA.

⁴Jet Propulsion Laboratory, California Institute of Technology, Pasadena, California, USA.

⁵Mauna Loa Observatory, National Atmospheric and Oceanic Administration, Hilo, Hawaii, USA.

⁶Los Gatos Research, Inc., Mountain View, California, USA.

⁷Picarro, Inc., Santa Clara, California, USA.

⁸Department of Applied Mathematics and Theoretical Physics, University of Cambridge, Cambridge, UK.

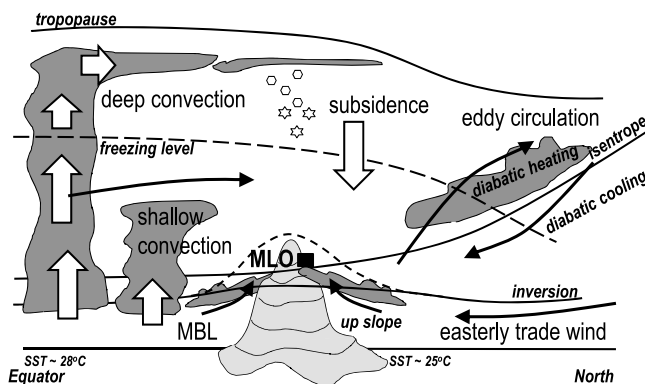


Figure 1. Schematic depiction of the water balance showing the location of the Mauna Loa Observatory. Water from the marine boundary layer can be exported through turbulent mixing at the MBL top, detrainment from shallow marine cumulus, or detrainment from deep, penetrative cumulus. Detrained ice crystals and cirrus clouds can ablate during their fall. Diabatic cooling drives large-scale descent, while latent heating causes slightly nonisentropic motion associated with eddies. Evaporation from the surrounding ocean ensures vapor within the MBL remains close to isotopic equilibrium with ocean water during trade conditions.

[3] Figure 1 is a schematic view of the water budget of the subtropical troposphere near Hawaii. The water vapor concentration above the subtropical boundary layer is low, and the relative humidity is typically less than 30%. The water vapor content of subtropical tropospheric air is well described if it is assumed that the vapor pressure of each member of the ensemble of parcels that compose the time mean is equal to the saturation vapor pressure experienced by that parcel the last time it encountered saturation along a backward Lagrangian path [Sherwood, 1996a; Pierrehumbert *et al.*, 2007]. Modeling studies have shown that the driest air is associated with approximately isentropic advective intrusions from higher latitudes where previous condensation at colder temperature has dried the air [Salathé and Hartmann, 1997; Pierrehumbert and Roca, 1998; Minschwaner and Dessler, 2004; Galewsky *et al.*, 2005; Cau *et al.*, 2007; Galewsky and Hurley, 2010], although dehydration associated with subsidence in the region of clouds in the tropics can also explain the distribution of relative humidity [Sherwood, 1996b; Ryoo *et al.*, 2009]. Opposing the dry air, moist filaments of equatorial origin are clearly visible in meteorological satellite images [McGuirk and Ulsh, 1990; Newell *et al.*, 1992; Pierrehumbert and Yang, 1993; Zhu and Newell, 1994]. These are associated with midlatitude cyclones that dominate moisture transport through the subtropics [Couhert *et al.*, 2010]. In Hawaii, these high-humidity filaments are associated with the frontal zone of cyclones and have been linked to the Kona Low and local high precipitation events [Morrison and Businger, 2001]. While the water vapor fluxes associated with large-scale and local transport phenomenon act intermittently, the balance that emerges in time-mean statistics describes the mean atmospheric hydrology of the region.

[4] Exchange of moisture between the marine boundary layer (MBL) and the free troposphere is limited in the subtropics because of the strong temperature inversion associated

with the trade winds [Albrecht, 1989; Chen and Feng, 2001]. Modeling studies show that exchange in subtropical regions is likely associated with detrainment from shallow convection rather than dry turbulent exchange [Bretherton *et al.*, 1995; Medeiros *et al.*, 2005]. Near the Big Island of Hawaii, topographic effects induce strong diurnal variations in the local trade inversion, and these are known to influence trace gas measurements and aerosols [Goldman, 1974; Weber and McMurry, 1996; Cao *et al.*, 2007]. However, the importance of the diurnal cycle in pumping MBL water across the inversion to the free troposphere is poorly understood.

[5] The hydrogen isotope ratios in water vapor are a function of equilibrium fractionation between vapor and condensed water, and kinetic fractionation associated with diffusion during condensation and evaporation [Bigeleisen, 1961; Merlivat and Jouzel, 1979]. In reference to Figure 1, isotopically different signatures emerge from the different hydrological history of air that has undergone dehydration at high latitudes, are associated with detrainment from clouds, or are dominated by evaporation from the ocean surface [Dansgaard, 1953; Jouzel, 1986; Gat, 1996]. Measurements of the isotope ratios of water vapor in the subtropical troposphere can therefore be used to help identify the mechanisms that control the subtropical humidity budget. Once air masses associated with the different processes are identified, statistics on their frequency can be used to provide new insight into the time-mean hydrological balance.

[6] The isotopic composition of precipitation has been used extensively for water cycle studies [e.g., Dansgaard, 1953; Gat, 1996; Coplen *et al.*, 2008], yet there are fewer that have utilized in situ measurements of the isotopic composition of vapor above the boundary layer. The technical challenges of aircraft-based measurements using cryogenic trapping [Ehhalt, 1974; Rozanski and Sonntag, 1982; He and Smith, 1999; Ehhalt *et al.*, 2005] or the need for specialized optical research instruments [Webster and Heymsfield, 2003; Kerstel *et al.*, 2006; Iannone *et al.*, 2010; Sayres *et al.*, 2010] have limited the availability of such data. Making reliable water vapor isotope estimates using high spectral resolution remote sensing from satellite-based [Worden *et al.*, 2006; Payne *et al.*, 2007; Worden *et al.*, 2007; Frankenberg *et al.*, 2009; Herbin *et al.*, 2009] and ground-based [Schneider *et al.*, 2010a] platforms has allowed much greater spatial and temporal coverage, albeit at limited precision and accuracy. With the advent of commercial water vapor isotopic analyzers using cavity-enhanced spectroscopic methods [Lis *et al.*, 2008; Gupta *et al.*, 2009], continuous time series data can be obtained and now places water vapor isotopologue composition into a meteorological context.

[7] Continuous measurements of isotopologues of water at Mauna Loa Observatory (MLO), Hawaii, were made for a 4 week period in October and November 2008 using cavity-enhanced spectroscopic methods. It is proposed that the subtropical measurements can be described as a sequence of mixing between distinct air masses that evolve with the synoptic conditions. The analysis seeks to (1) explain the isotope variations associated with the diurnal transitions between boundary layer and free tropospheric air, (2) explain the variations in the nighttime (free tropospheric) observations on the basis of the large-scale meteorology, and (3) demonstrate the unique information that can be discerned from isotope ratio measurements. The synoptic-scale flow is

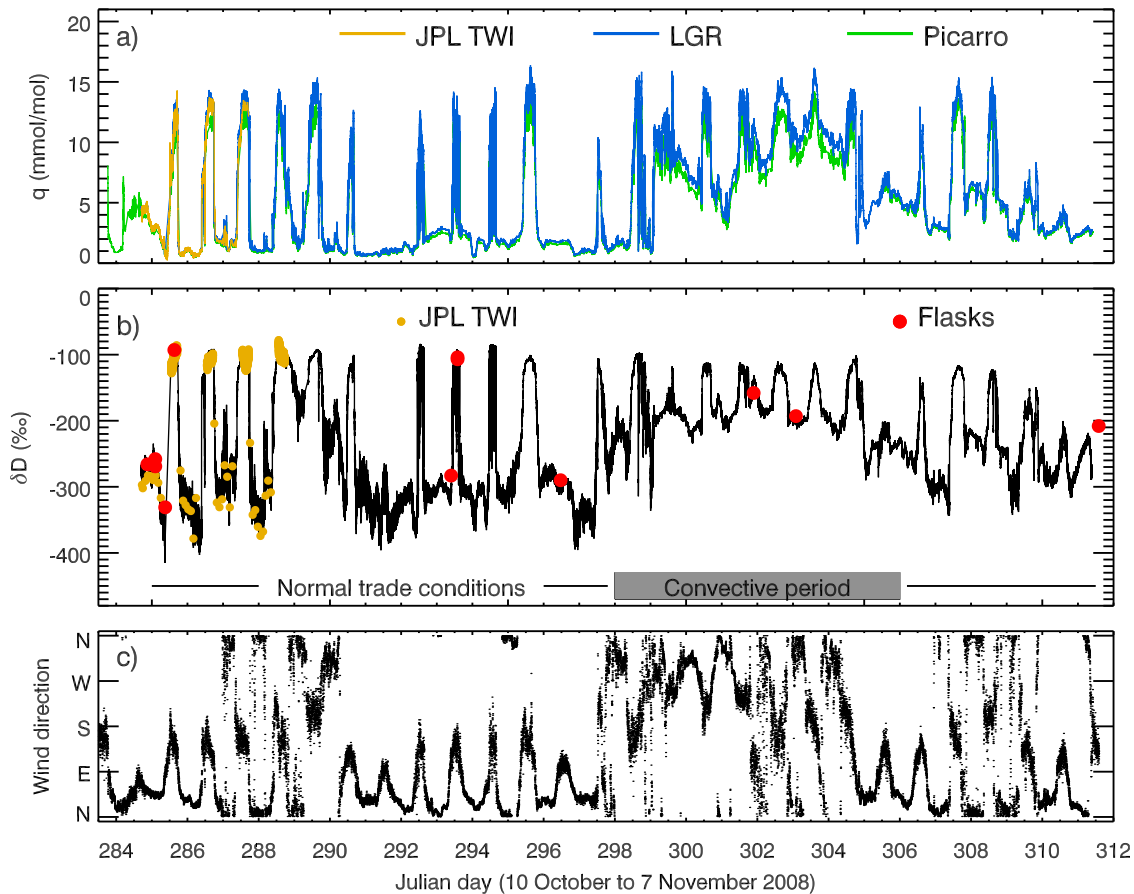


Figure 2. Time series of (a) water vapor volume mixing ratio, (b) δD of water vapor, and (c) direction at Mauna Loa from 10 October to 7 November 2008. Figure 2a shows data from the LGR water vapor isotope analyzer (blue), Picarro isotopic water vapor analyzer (green), and JPL-TWI (orange) instruments. Figure 2b shows the single calibrated isotope record based on the LGR data set (black). Also shown are data from the JPL-TWI (orange dots) and flasks (red dots). The gray box differentiates the convective period between days 298 and 306 from the remainder of the record when normal easterly trade conditions dominate.

characterized using back trajectories to help determine the air mass histories and separate the role of slow subsidence in the subtropics from horizontal transport associated with mid-latitude eddies and from convection. Water exchanges are described with a mixing-line analysis that exposes the unique insight offered by paired measurements of H_2O mixing ratios and D/H isotope ratios. Section 2 describes the water vapor isotopic data set that comprises D/H isotope ratios of water vapor from three spectroscopic instruments.

2. Data and Methods

2.1. Isotope Measurements at Mauna Loa

[8] The concentration of H_2O and HDO isotopologues in vapor phase were measured at the NOAA observatory at Mauna Loa, Hawaii ($19^\circ 30'N$, $155^\circ 35'W$, 3397 meters above sea level), between 10 October and 6 November 2008 (Figure 2). Isotopic data are reported in the standard δ notation given by

$$\delta D = \frac{R}{R_{std}} - 1, \quad (1)$$

where $R = D/H$ for δD . All data are reported relative to Vienna SMOW (VSMOW), defined as $\delta D \equiv 0\text{‰}$ for VSMOW and $\delta D = -428\text{‰}$ for standard light Antarctic precipitation [Coplen, 1995].

[9] A Los Gatos Research Incorporated (LGR) water vapor isotope analyzer (which uses an off-axis cavity-enhanced spectroscopic method [Lis *et al.*, 2008]) and a Picarro Incorporated isotopic water vapor analyzer (which uses a wavelength scanning cavity ring-down method [Gupta *et al.*, 2009]) were deployed over the entire sampling period. For the first 5 days of the experiment, the NASA Jet Propulsion Laboratory Total Water Instrument (JPL-TWI) (adapted from the high-altitude “ALIAS” instrument used by Webster and Heymsfield [2003]) was also used. All instruments drew air from an intake less than 1 m above the roofline of the laboratory and used unheated 0.25 inch tubing that spanned between 5 and 10 m to the bench-mounted instruments. The Picarro and JPL-TWI used stainless steel and the LGR used Teflon tubing. The laboratory was heated/air conditioned at a temperature of around $20^\circ C$ with fluctuations on the order of $5^\circ C$. Since the laboratory was warm, and the ambient relative humidity was generally low, there was no

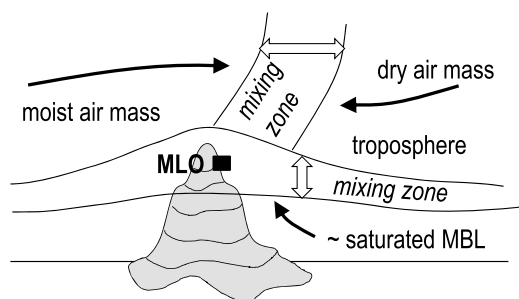


Figure 3. Schematic depiction of air mass mixing zones (open arrows). Vertical mixing zones between the MBL and the troposphere and lateral mixing zones in the troposphere separate distinct air masses as they pass across MLO and allow the station time series measurements to capture the spatial mixing gradients.

condensation in the inlet lines. The LGR instrument recorded measurements at 2 Hz (with 10 s averages reported here), the Picarro instrument reported measurements every 6 s, and the JPL-TWI made measurements every second (with 30 min averages reported here). Laboratory tests of more recent Picarro and LGR instruments suggest they have a response time on the order of 1 min. For the first generation of commercial instruments used in this study, the manufacturer specification indicates that the precision (1 standard deviation repeatability) of the measurements is 0.2‰ for 5 min averages for LGR at humidity greater than 4 mmol/mol H₂O and is 1‰ between 5 and 20 mmol/mol H₂O for Picarro. Experience from this field experiment suggests that these estimates are robust, but the precision is lower at the lower water concentration observed at nighttime at MLO (for instance, at 0.5 mmol/mol, the Picarro precision is about 18‰). Furthermore, special care is needed to ensure calibration to the absolute (VSMOW) scale (see below).

[10] Calibration of the isotopic analyzers employed a two-step approach: (1) data were calibrated against periodic measurement of known standards to remove any drift; and (2) a correction was applied to match the data obtained from mass spectrometric measurement of whole air flask samples. Calibration of the LGR analyzer occurred every 5 h and was based on measurement of vapor with a known isotopic composition that had been set via equilibration with a single liquid pool in a dew point generator. The instrument sensitivity was preset in the laboratory and the single calibration used to correct for biases and drift. The value measured could be matched to the values expected after fractionation at the prescribed temperature and the (known) isotopic composition of the liquid reservoir. Calibration of the Picarro analyzer occurred every 6–8 h and was based on injection of three liquid standards using an autosampler with complete vaporization into dry air [Gupta *et al.*, 2009]. This allowed both instrument drift and the absolute calibration to be accounted for at a particular humidity. Calibration of the JPL-TWI occurred prior to the field experiment at the NASA JPL by completely vaporizing water of known isotopic composition into a stream of dry air. The JPL-TWI measurement, although only spanning the first 5 days of the campaign, is included to compare the untested commercial analyzers with an established research instrument.

[11] It was found that the early generation of LGR and Picarro analyzers used in this experiment has a measurement dependence on humidity, which is particularly strong at a low H₂O concentration. While this has been partially addressed in more recent versions of the commercial instruments, the field calibration practices employed in the 2008 experiment did not include an account of humidity dependence, and so a posterior correction of the data was required. The correction was based on matching the spectroscopic δD measurements to values obtained by mass spectrometer analysis of vapor collected in glass vacuum flasks. Whole air samples were collected using 2000 ml glass vacuum flasks [Strong *et al.*, 2007]. The flasks were returned to the University of New Mexico, and the D/H ratio was determined using laboratory techniques that have been demonstrated to yield robust and repeatable measurement of the true D/H ratio irrespective of ambient water [Johnson *et al.*, 2011] (Figure 2b, red dots). These flask data provide a benchmark against which the D/H ratio obtained spectroscopically can be adjusted to the VSMOW scale over the humidity range measured. The correction is a scaling of the spectroscopic measurements based on a linear relationship between the spectroscopic estimates and the known value from 12 flasks. By design, this correction brings the LGR and Picarro measurements into agreement within the statistical uncertainty of the humidity-dependent calibration curve [see Johnson *et al.*, 2011].

[12] The flask method was not able to give measurements of the ¹⁸O/¹⁶O isotope ratio. Similarly, vapor collected as condensate using cryogenic traps (cooled to −78°C with a mixture of denatured alcohol and dry ice) was found to be of poor quality and, consequently, could not provide a reference for calibration. Therefore, measurements of the ¹⁸O/¹⁶O ratio made with the laser spectrometers could not be calibrated to the level needed for reliable deuterium excess values, and only the δD values are reported here.

[13] A Licor 7000 Infrared Gas Analyzer measured CO₂ and total water mixing ratio at 2 Hz to provide checks on any local air mass contamination and to provide an independent reference for the H₂O measured by laser spectroscopic measurements. The precision of the H₂O measurement from the Licor is 20 ppm, and the accuracy is 1% compared to zero-grade dry air in the reference cell. Spikes in the CO₂ concentration were associated with automobile traffic in the observatory parking lot and air that escaped from within the observatory buildings when doors were opened. The corresponding isotopic data were removed from the time series to avoid any potential contamination.

2.2. The Isotopic Signature of Air Mass Mixing

[14] The observations capture mixing in the region of frontal transitions between air masses, shown schematically in Figure 3. Assuming that variations in mixing ratios (either H₂O or HDO) in the frontal mixing zone are governed by turbulence, the evolution of the mixing ratio is

$$\frac{\partial q}{\partial t} = K \frac{\partial^2 q}{\partial x^2}, \quad (2)$$

where K is an eddy diffusivity (assumed constant for simplicity) and x is a spatial coordinate in the direction

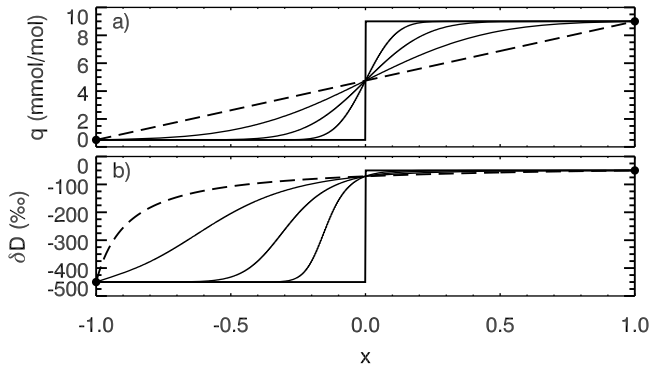


Figure 4. Solutions to the diffusion mixing model for (a) q and (b) δD as a function of space at different times for the case for mixing between two air masses. Boundary conditions are $q_1 = 0.5$, $\delta D_1 = -450\text{‰}$ and $q_0 = 9.5$ and $\delta D_2 = -100\text{‰}$ (solid dots). The initial condition is a “step” function with values $q = q_1$ and q_2 , and $\delta D = \delta D_1$ and δD_2 with a discontinuity at $x = 0$ (bold). The curves are generated numerically using second-order finite differences with a diffusion coefficient, $K = 1$, on a domain with 1000 equally spaced points and a time step $\Delta t = 0.5\Delta x^2/K$. Curves are plotted showing transient solutions at time $t = 0.001, 0.004$, and 0.016 (solid curves). The steady state solution (dashed curve) shows the hyperbolic profile in space.

of the maximum gradient (vertical or horizontal). The solution is

$$q = q_0 + (q_1 - q_0) \times \frac{1}{2} \left[1 + \operatorname{erf} \left(\frac{x}{\sqrt{4Kt}} \right) \right], \quad (3)$$

where erf is the Gauss error function and the term in square brackets divided by 2 is a number between 0 and 1 for a particular value of x and t . (It is often convenient to define the observed quantity as the weighted mean of the two end members. Specifically,

$$q = (1 - f)q_0 + fq_1$$

$$f = \frac{1}{2} \left[1 + \operatorname{erf} \left(\frac{x}{\sqrt{4Kt}} \right) \right],$$

If q_0 and q_1 are known, f can be determined from measurements, as indicated on the top axis in Figure 6.) A similar expression can be written for the minor isotope species and the isotope ratio found. Some solutions for q and δD are shown in Figure 4 in the case of mixing at the intersection of two air masses with fixed properties $q_0, \delta D_0$ at $x = -1$ and $q_1, \delta D_1$ at $x = 1$. Values are chosen to be typical of the measurements at Mauna Loa. The air masses are initially unmixed, and as time passes, diffusion establishes a gradient across the mixing zone defined by the domain width. The structure of the curves is symmetric about the domain center for q . Asymmetry in δD results because the isotopic ratio of the air with higher q values dominates the mass balance. (Adding a small amount of yellow water to a large amount of blue water does not change the color green, but combining a small amount of blue water with a small amount of yellow water does.) This asymmetry is the feature of importance because it

demonstrates the information in δD that is different from that of q .

[15] Equation (3) is expressed as the sum of the initial value q_0 , plus some “flux.” That is,

$$q = q_0 + q_F \quad (4)$$

$$Rq = R_0q_0 + R_Fq_F,$$

where R is the isotope ratio. Upon rearranging and using (1),

$$\delta D = q_0[\delta D_0 - \delta D_F] \left(\frac{1}{q} \right) + \delta D_F, \quad (5)$$

and from (3),

$$\delta D_F = \frac{\delta D_1 q_1 - \delta D_0 q_0}{q_1 - q_0}. \quad (6)$$

[16] This shows that mixing between two end-members will trace a straight line when plotted as δD versus the reciprocal of the water vapor mixing ratio, q^{-1} . The result is similar to the one-box approach used to identify the source of terrestrial ecosystem carbon fluxes from carbon isotope ratio time series data [Keeling, 1958; Miller and Tans, 2003]. An analogous case for water vapor is the surface flux associated with evaporation from the ocean, where δD_F is the isotopic composition of the evaporative flux. The general solution (3) describes this case where the flux associated with evaporation from the ocean is a boundary condition $q_1, \delta D_1$ (Figure 5). Following Craig and Gordon [1965], the isotopic composition of evaporation flux is modeled as $\delta D_e = (\delta D_s - \delta D h) / (1 - h) - \varepsilon_k$, where δD_s is the delta value of vapor in equilibrium with ocean liquid, h is the relative humidity (for saturation at the liquid skin temperature), and ε_k is the kinetic fractionation and is similar in form to (6). Agreement with (4) and (6) results assuming $\varepsilon_k = 0$, $h = q/q_0$, and $\delta D_1 = \delta D_s$. In general, δD_F is not the same as the isotopic composition of the end-member δD_1 , and it is left as an analysis task to interpret δD_F .

[17] The proof here demonstrates that the hyperbolic relationship between δD and q (notice the q^{-1} in equation (5)) is

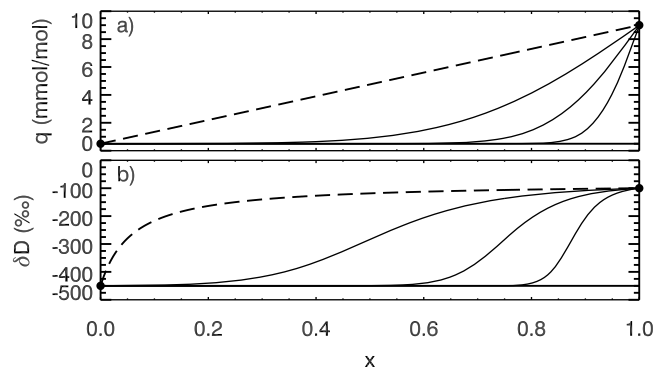


Figure 5. As in Figure 4 but for the case where the initial conditions are $q = q_0$ and $\delta D = \delta D_0$ (bold). The steady state solution is dashed, and the same hyperbolic shape as in Figure 4 is seen in Figure 5b. Curves are plotted showing transient solutions time $t = 0.002, 0.008$, and 0.032 (solid curves).

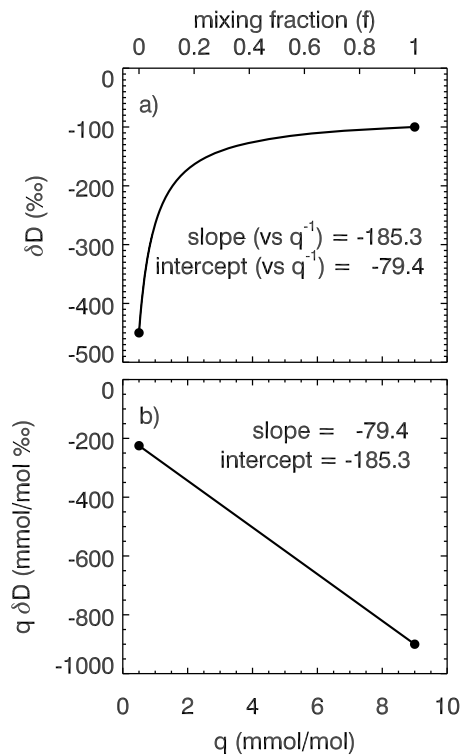


Figure 6. Relationship between q and δ for the diffusive mixing model, (a) δ as a function of q^{-1} and (b) $q\delta$ as a function of q . Solid dots show the two end points q_0, δ_0 and q_1, δ_1 . All q, δ values (all times, all locations) for both the case of free air mixing or mixing at the restorative boundary fall along the same line. The top axis shows the linear relationship between f and q in Figure 6a, where $f = 0$ at $q = q_0$ and $f = 1$ at $q = q_1$. Moistening causes displacement to the right, and drying causes displacement to the left, and the q - δ value remains on the line with the same slope.

exceedingly general and valid for both space and time problems. Figure 6a shows the hyperbolic curve, and it is the same curve if the model solutions are plotted either as time series or spatial variations, and it is also the same curve for both the free air cases (Figure 4) or the surface flux case (Figure 5). In the case of Mauna Loa data, the time series observations largely sample the spatial gradient as the fronts move past the station and the transitions between air masses are observed (Figure 3). In the case of deforming flow or if there are additional moisture sources or sinks, (2) is no longer valid, and an alternate model must be used.

[18] Two pieces of information can be obtained from measurements with the mixing model that cannot be obtained from measurements of q alone. First, if observations lie along a hyperbolic path traced on a q - δD plot, air mass mixing can be identified. Other processes, such as condensation, do not follow a hyperbolic path (a Rayleigh model, for instance, predicts a logarithmic curve) and can be ruled out. Second, the δD value of the flux (δD_F) can be obtained by regressing the observations in which mixing has been identified to the mixing model. Equation (5) has the form $y = ax + b$, where x is q^{-1} and b is δD_F [Keeling, 1958]. However, regressing against q^{-1} can introduce large type-2 fitting errors that can

be reduced if (5) is rearranged [see Miller and Tans, 2003] to be

$$\delta D q = \delta D_F (q - q_0) + \delta D_0 q_0, \quad (7)$$

which again is a linear model in which δD_F is found as the slope (compare Figures 6a and 6b). δD_0 cannot be found unless q_0 is known. However, δD_F provides a single measure that characterizes the water fluxes.

[19] In the MLO data, periods when the observations are associated with air mass mixing are identified when the evolution of the time series of q and δD is well described by the mixing model (i.e., the data would form a line on a $q\delta D$ versus q plot). Each 1 h window of the time series data is flagged as sampling a mixing process if the square of the correlation between $q\delta D$ and q exceeds 0.8 and the magnitude of the correlation is larger than between δD and q , or δD and the natural logarithm of q , which is associated with condensation (D. Noone, Pairing measurements of the water vapor isotope ratio with humidity to deduce atmospheric moistening and dehydration in the tropical mid-troposphere, submitted to *Journal of Climate*, 2011). Once the mixing events are identified, δD_F is derived from regression in the form of (7). This algorithm provides an objective method for detecting mixing lines in the time series data without a priori selection or subjective subsetting of data. A similar approach was used to evaluate mixing in the continental boundary layer by searching for sections of vertical profile isotope data that fit a mixing model [He and Smith, 1999].

2.3. Other Data and Methods

[20] Complementing the isotopic measurements, meteorological conditions (temperature, dew point temperature, wind speed, direction, and station pressure) are taken from the NOAA station observations at MLO. Radiosonde data from twice-daily launches at Hilo were obtained from the NOAA Forecast Simulation Laboratory archive (<http://www.esrl.noaa.gov/raobs/>). Hilo is approximately 50 km to the east of MLO. Precipitable water estimates are from version 5 of the NASA Atmospheric Infrared Sounder Level 3 standard retrieval data product gridded on a 1° regular grid (<http://disc.sci.gsfc.nasa.gov>). The data presented are the mean of the ascending and descending orbits as a proxy for the daily mean.

[21] Three-dimensional kinematic back trajectories [Noone and Simmonds, 1999; Noone et al., 1999] were calculated from the NCEP/NCAR Reanalysis data [Kalnay et al., 1996]. Vertical velocity was calculated diagnostically using the continuity equation on “sigma” coordinate surfaces based on the horizontal divergence and surface pressure tendency fields available as spherical harmonic coefficients in the archive at the National Center for Atmospheric Research. The trajectory algorithm uses tricubic interpolation in space and linear interpolation in time to obtain wind and tracer quantities at trajectory locations. Temperature, geopotential height, and specific humidity are interpolated to the trajectory locations and used to compute the moist and dry static energy along the transport path. Time stepping uses a fourth-order Runge-Kutta scheme to obtain accurate back trajectory paths over integrations of 5–10 days. Trajectory dispersion is checked using multiple launches displaced from the Hawaii arrival point by 20 km in each compass direction and at

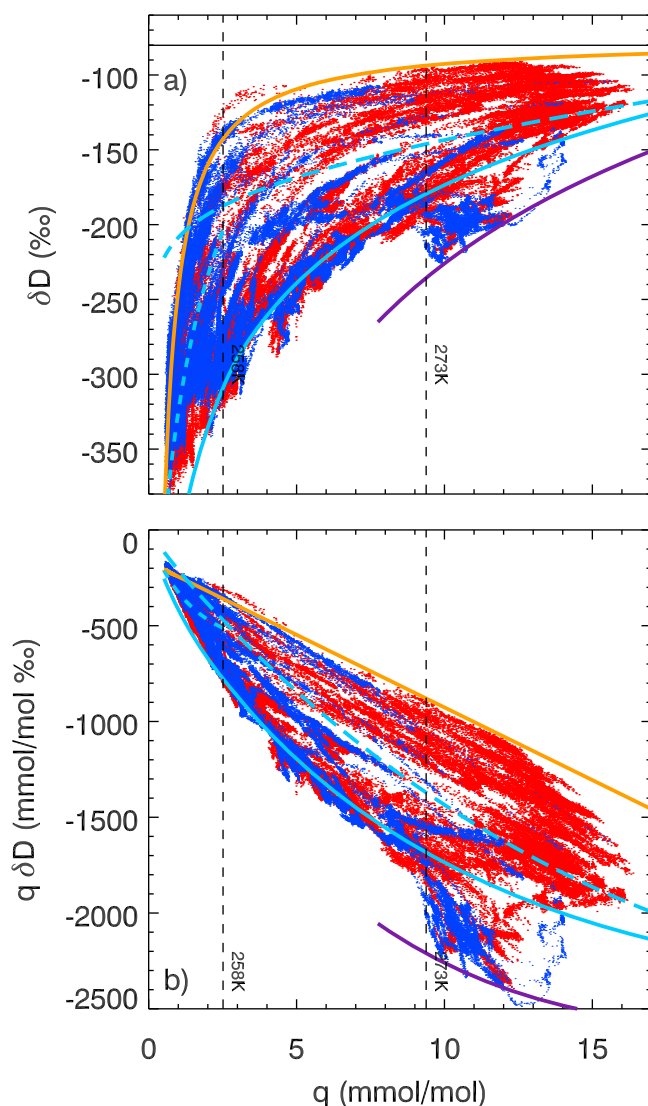


Figure 7. All calibrated measurements of δD at MLO: (a) δD versus water mixing ratio (q) and (b) $q\delta D$ versus q , as in Figure 6. Daytime data (0600 to 1800 HAST) are shown in red, and nighttime data (1800 to 0600 HAST) are in blue. Curves are for reversible moist adiabatic processes (dashed cyan), pseudoadiabatic/Rayleigh processes (solid cyan), super-Rayleigh processes (such as accompany exchange during rain evaporation; purple), and a mixing between the troposphere and water saturated at the ocean surface (orange). Dashed vertical lines indicate the saturation mixing ratio at 273 and 258 K. The curves assume a source at 80% relative humidity over an ocean at 25°C, as is typical in the subtropical MBL. Mixing between any two air masses plots a straight line in Figure 7b.

various launch heights. Only results from a single launch altitude and time are reported for the sake of clarity.

3. Results

3.1. Features of the Measured Time Series

[22] Figure 2 shows the dominant role of the diurnal cycle over the course of the experiment. Water vapor mixing ratios

were typically around 12 mmol/mol (12,000 ppm) during the day and often between 0.5 and 1 mmol/mol (500–1000 ppm) at night. Nighttime values capture the regional synoptic influences in the troposphere, while daytime values are associated with upslope flow and reflect the dominant influence of MBL air [Goldman, 1974]. Without any post-calibration, the LGR, Picarro, and JPL-TWI water vapor mixing ratio measurements are very similar (Figure 2a). The RMS difference between the LGR and Picarro measurements is 0.5 mmol/mol and is dominated by differences at high frequencies during transitions from high to low water concentration, which may partially be associated with differences in the response time of the different instruments and inlet lines.

[23] The isotope ratio data exhibit similar diurnal variability as the H_2O mixing ratio. Daytime δD values are typically around -100‰ , and the driest nighttime air has δD values around -400‰ . As with the water vapor mixing ratio, the three spectroscopic records of isotopic composition are remarkably similar. The differences in the δD values reported directly by the instruments (i.e., without calibration) can be 30‰. However, after applying the calibration against the whole air flask samples, the results from the two commercial instruments are very similar. The RMS difference is 18‰ for the whole data set and 11‰ where $q > 5$ mmol/mol [Johnson *et al.*, 2011]. Since the records from both the LGR and Picarro analyzers are similar, only the results from the LGR analyzer are used hereafter (blue curve in Figure 2a and black curve in Figure 2b, and preferred to the Picarro data, which has a 26 h gap on day 305 due to a stall in the calibration procedure). The agreement with the separately calibrated JPL-TWI during the first 5 days provides confidence in the flask-based calibration procedure.

[24] Figure 7a shows that nearly all individual (10 s average) observations fit within the set of theoretical curves in q - δD space for simple systems [Worden *et al.*, 2007; Noone, submitted manuscript, 2011]. The individual curves are of well-known “box models” for isotope processes [e.g., Keeling, 1958; Craig and Gordon, 1965; Jouzel, 1986; Gat, 1996]. The measurements are bounded on the low δD value side of the distribution by a curve that models pseudoadiabatic condensation and isotopic rainout (as in the Rayleigh distillation; Figure 7, cyan curve) and bounded on the high δD value side of the distribution by a curve that models moistening by evaporation from the ocean surface (i.e., mixing with the moist end-member that is vapor in isotopic and thermodynamic equilibrium with ocean water and a dry end-member chosen to be representative of the driest observations; Figure 7, orange curve). High daytime water mixing ratio values suggest a strong influence of surface evaporation in the MBL, which also has high δD values, and it remains to quantitatively demonstrate that the origin of these changes is a source with an isotope ratio consistent with MBL air. The theoretical curves show that the low q and low δD values observed at night can result from either pseudoadiabatic rainout (high precipitation efficiency is described as a Rayleigh process) or reversible (“warm rain”) processes (i.e., the “closed” isotope model, with near-zero precipitation efficiency; Figure 7, dashed cyan curve) until the frost point followed by rainout associated with ice condensation. The frost point is taken below freezing to account

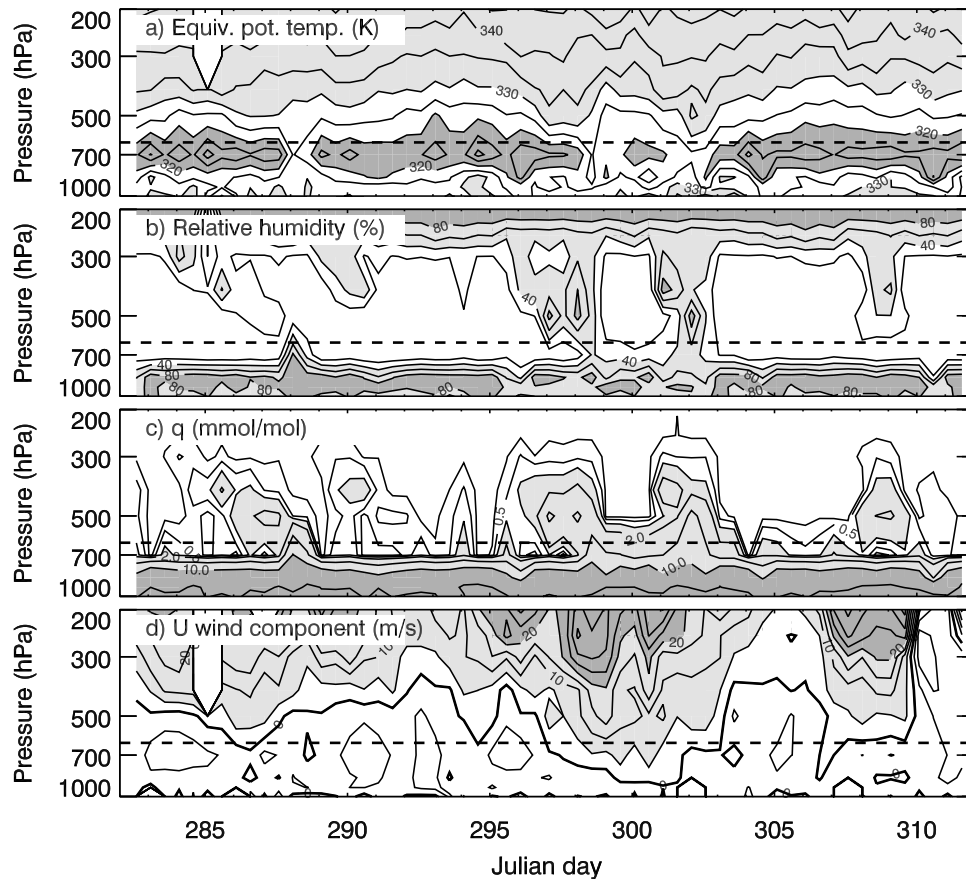


Figure 8. Radiosonde observations from twice-daily soundings launched at Hilo of (a) equivalent potential temperature, (b) relative humidity, (c) water vapor volume mixing ratio (q), and (d) the westerly wind component. The contour interval is 5 K in Figure 8a; 20% in Figure 8b; in decades of 1, 2, and 5 mmol/mol in Figure 8c; and 5 ms^{-1} in Figure 8d. The zero contour is bold in Figure 8d. The horizontal dashed line is the typical pressure of MLO. The mid and upper tropospheric values are recorded and can be significantly downwind of Hilo because of the wind drift of the balloon. The relative humidity values above 300 hPa are biased high in association with known instrument errors of the sondes.

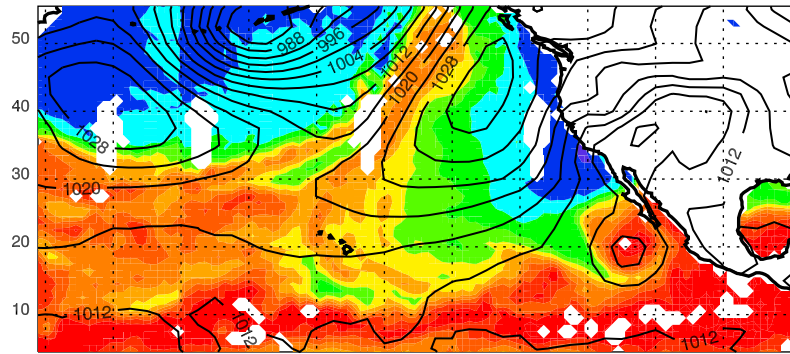
for mixed-phase clouds. The observations capture a distinct air mass that has δD values that are lower than can be explained by a Rayleigh distillation given the water mixing ratio of around 11 mmol/mol. These observations are consistent with either the influences of isotopic exchange that are expected during evaporation of falling rain (i.e., a super-Rayleigh distillation; Figure 7, purple curve) or if the origin of the moisture is the surface ocean at 30°C–32°C. While rain evaporation occurs everywhere, Tropospheric Emission Spectrometer (TES) data show its prevalence in the equatorial region (Noone, submitted manuscript, 2011). Therefore, both possible explanations for these low δD value observations suggest water originating from the deep tropics.

[25] Figure 7b shows the same data plotted as $q\delta D$ versus q , as in Figure 6b. Inspection reveals sections of data that appear to lie along straight lines. Given the theory developed above, these can be interpreted as periods when there is mixing at the transition between different air masses. A quantification of these exchanges is given below and made by counting the frequency with which mixing lines appear and by examining the value of δD_F .

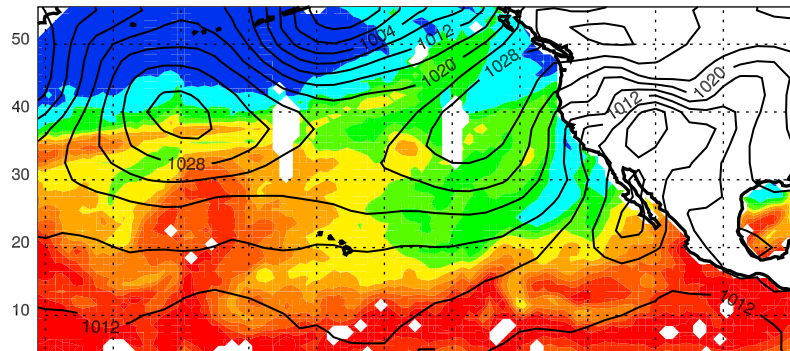
3.2. Influence of Large-Scale Circulation

[26] To first order the isotope ratios act as a tracer of air mass origin. Figure 2 shows a change in the character of the time series between days 298 and 305. The station wind direction changes from predominant easterly/northeasterly flow associated with normal trade conditions in the early part of the record to a period of westerly flow (Figure 2c). Hilo radiosonde observations (Figure 8) show that the transition to westerly flow is a downward extension of the upper and midtropospheric westerly flow, although the wind speed at the station height remained less than 10 m/s (note the zero contour in Figure 8d). This enhanced westerly flow persists in the region for around 7 days. During this time, high water vapor mixing ratio values are observed throughout the lower troposphere. The minimum in equivalent potential temperature that is usually sustained by subtropical subsidence during trade conditions is diminished (Figure 8a). The high relative humidity through the troposphere (Figure 8b) suggests the atmosphere is close to moist adiabatically stratified and is an indication of the strong influence that recent convective activity has had on the observed air mass. Hereafter, this is referred to as the convective period of the time series. The

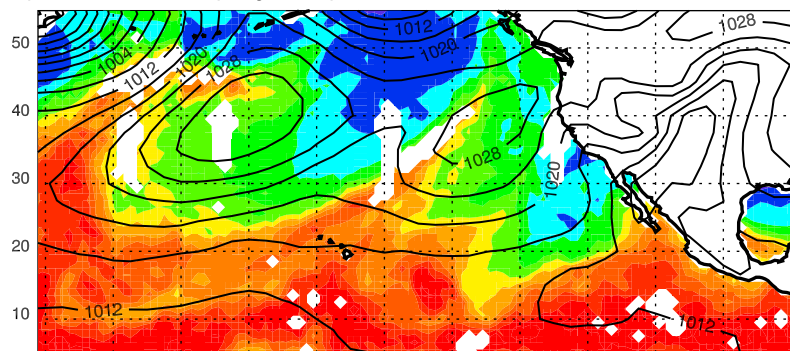
a) 11 October (day 285)



b) 18 October (day 292)



c) 29 October (day 303)



d) 2 November (day 307)

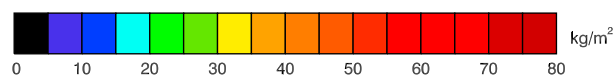
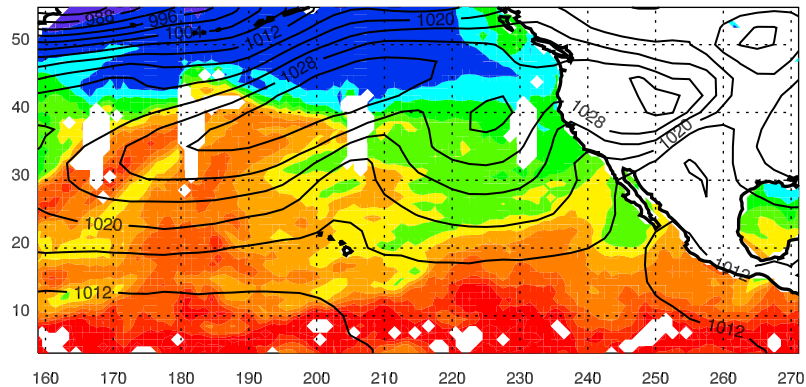


Figure 9

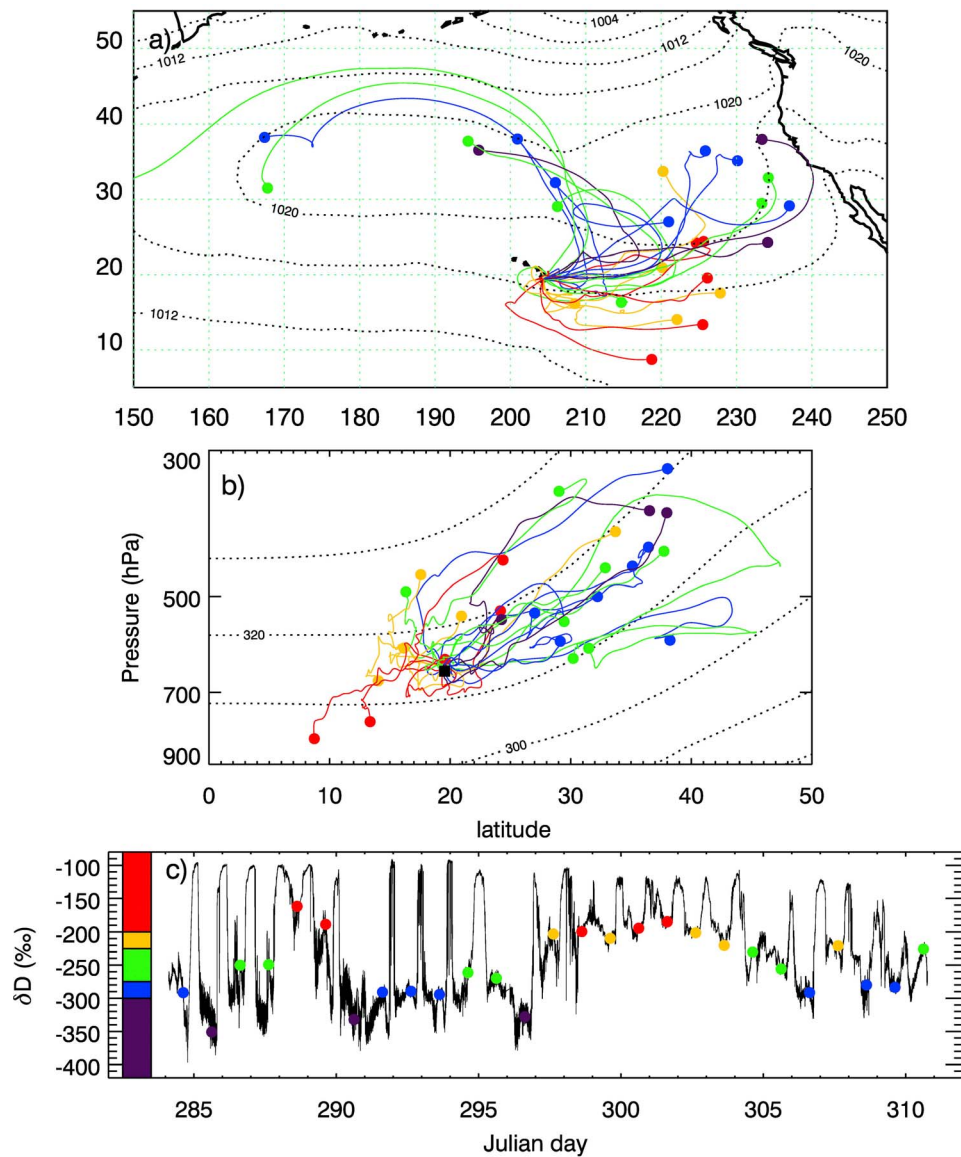


Figure 10. Six-day kinematic back trajectory paths for parcels launched at midnight (local) showing (a) horizontal and (b) vertical displacements, and (c) the time series of δD as in Figure 2b. Trajectories and 6 day position are colored based on the δD value observed at MLO as indicated in Figure 10c. In Figure 10b, the location of MLO is shown as a black square. The 10 October to 6 November average mean sea level pressure is shown in Figure 10a (dashed curves, contour interval of 4 hPa), and potential temperature in Figure 10b (dashed curves, contour interval 5 K) are from the NCEP/NCAR Reanalysis.

flow changes back to easterly trade conditions on day 306, and the prominent diurnal cycles reappear.

[27] Maps of precipitable water derived from infrared satellite observations show that, during the early part of the experiment, Hawaii was situated in a broad region of dry air intruding from the northeast that was to the east of a frontal zone in the midlatitudes (Figures 9a and 9b). During the

convective period event, a moist filament of equatorial origin with a zonally broad base is observed in the region near and to the south of Hawaii (Figure 9c), and both nighttime and daytime isotope ratio observations are influenced (recall Figure 2). Evidence for the air associated with the convective period at MLO terminates abruptly as the north Pacific circulation changes to anticyclonic flow (Figure 9d). Easterly

Figure 9. Daily average column integrated precipitable water from Atmospheric Infrared Sounder/advanced microwave sounding unit on (a) 11 October, (b) 18 October, (c) 29 October during the convective period, and (d) 2 November. Dates are given as UTC. Data are the average of ascending and descending orbits that occur at around 0130 and 1330 local equatorial crossing time. Missing data are due to clouds and gaps associated with the orbit track. Contours show daily average sea level pressure from the NCEP/NCAR Reanalysis (interval of 4 hPa).

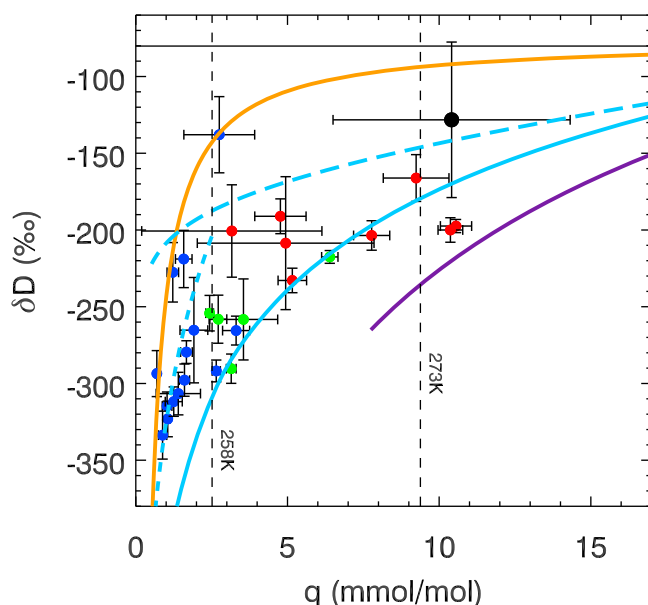


Figure 11. As in Figure 7a but for average nighttime (2300 and 0300 HAST) and daytime (1300 and 1500 HAST) values. Average δD values are mass weighted. Nighttime averages are shown for each day for the normal trade conditions (blue dots, before day 298; green dots, after day 306) and for the convective period (red dots, between days 298 and 306). Daytime values are the average of all days (black dot). Error bars indicate the 1 standard deviation of 10 s measurements that comprise the mean to show the range of variability, rather than the uncertainty, in the estimate of the mean.

flow is reestablished with marine trade conditions, and the pronounced diurnal variability in the water vapor and δD values resume at MLO.

[28] Figure 10 shows results from a 6 day back trajectory calculation for parcels initialized at local midnight (1000 UTC) on each day of the experiment at an altitude of 630 hPa (approximate MLO station height). The trajectories capture the evolving organized large-scale flow and show that the isotope ratios in the free troposphere principally vary in association with the differences in air mass histories. Figure 10 reveals that the dry and lower δD value air masses are associated with the weak anticyclonic flow ahead of the convective period and have origins upstream to the east and north (Figure 10, blue curves). These dry air masses tend to descend approximately isentropically from the mid-troposphere to the altitude of MLO. This is consistent with the prediction that the driest air in the subtropics is associated with condensation upstream at higher latitudes [e.g., *Pierrehumbert and Roca*, 1998; *Hurley and Galewsky*, 2010]. The trajectories associated with higher δD observations, such as during the convective period, differ in that they have a more equatorial origin (Figure 10, red and orange curves). Some of these high δD -value observations are associated with ascent (Figure 10b) prior to arrival at MLO. Although the trajectory calculation does not resolve convective transport, the moist static energy along trajectories during the convective period remains roughly constant (less than 0.5 K change in equivalent potential temperature), as expected, given the equivalent potential temperature dis-

tribution (recall Figure 8a). This approximate conservation of moist entropy shows that latent heating associated with convective activity upstream drives the ascent captured by the trajectories. Trajectories associated with intermediate δD values (Figure 10, green curves) tend to be associated with weak trade conditions such as the period following the convective period when the anticyclonic flow was weak.

[29] Figure 11 shows mean nighttime observations (average of 2300–0300 Hawaii–Aleutian Standard Time (HAST) observations) as a function of q . Analyzed this way, the unique information provided by the δD measurements emerges since different values of δD can discriminate between air masses with the same value of q . The lowest δD values (less than -300‰) are higher than the Rayleigh curves at around 0.5–2 mmol/mol and indicate the precipitation efficiency is less than 1. Below the frost point, some of these points fall along a Rayleigh curve with a slope associated with ice condensation, suggesting a history in which ice cloud forms from in situ deposition of vapor rather than the freezing of liquid that would be associated with convective updrafts. Below the frost point, the ice condensate cannot exchange with vapor, and further condensation drying would follow a Rayleigh-like history. Air that has been isentropically displaced poleward to high altitudes will reach sufficiently cold temperatures for glaciation, which provides a qualitative explanation of the dry region joint q - δD distribution.

[30] High δD values are typical during the convective period and suggest low precipitation efficiency. However, on two nights during the convective period, δD values are lower than can be explained by Rayleigh distillation (recall the super-Rayleigh curve shown in Figure 7), which suggests reprocessing of moisture by rain evaporation near clouds. Similar evidence for postcondensational exchange was found using TES satellite observations of HDO and H₂O and was suggested as a label for vapor with equatorial origin (Noone, submitted manuscript, 2011). On the other hand, a water source that is saturated above an ocean surface at 32°C can also match these observations if the cloud behaves pseudoadiabatically and a Rayleigh model is used. This is less likely given the typical distribution of very high sea surface temperatures, yet cannot be ruled out from the isotopic data alone. The origin of these observations is confirmed with the back trajectories shown in Figure 10 as the red points that originate to the south of Hawaii. At these locations, the ocean surface temperature was less than 28°C during the month of the experiment.

[31] Together, all points describe three or four distinct air masses that are associated with large-scale circulation features. Whether water vapor is exchanged at the transitions between the different air masses or whether the air masses remain hydrologically isolated from one another can be determined by the mixing line analysis.

3.3. Diurnal Variations and the Marine Boundary Layer

[32] Figure 12 shows the mean diurnal water vapor mixing ratio and the isotopic delta value binned to 10 min averages over the 28 days of the experiment. The mass weighted mean δD shows that nighttime values are $\sim 150\text{‰}$ lower than during the day in the normal trade wind conditions and $\sim 90\text{‰}$ lower during the convective period. While there is substantial day-to-day variation, there is a consistent

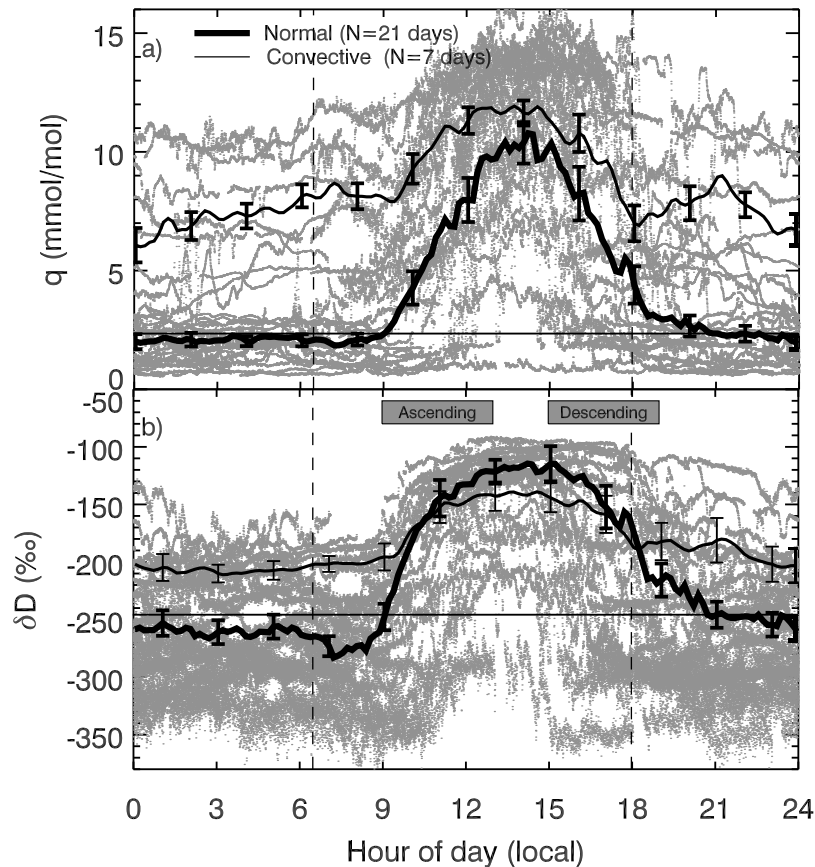


Figure 12. Mean diurnal cycle of (a) q and (b) δD as a function of local hour. The mean of data from the moist period between days 298 and 306 is shown (thin black curve) separately from all other data (thick curve). Gray dots show all observations over the 28 days of the experiment. Error bars show the standard error uncertainty on the mean (σ/\sqrt{N} , where $N = 7$ days for the convective period and $N = 21$ otherwise). Vertical dashed lines indicate typical sunrise (0623 HAST) and sunset (1804 HAST) times in Hawaii during October. The horizontal line shows the value of q and δD at 2100 HAST.

and fairly rapid transition from low to high values beginning at around 0900 HAST. The highest water vapor mixing ratios are observed at around 1330 HAST, followed by a slower return to low nighttime values in the evening. The timing of the evening transition is less regular than in the morning and continues beyond local sunset. Observations after ~ 2100 HAST are typical of the nighttime values and can be assumed to be the free troposphere.

[33] The appearance of MBL air in the morning is seen by an observer at MLO in connection with a layer of stratus cloud that rises slowly from the east after sunrise and moves upward along the orographic rise in the valley between Mauna Loa and Mauna Kea to the observatory. On 3 days of the experiment, the MBL air did not rise to the level of the MLO (δD values remain less than -200‰ on days 291, 295, and 305 in Figure 2b). The upslope air mass can be identified in station data as a shift in wind direction from the nighttime northeasterly flow to southeasterly (Figure 2c). This is a well-known meteorological phenomenon at MLO [Cao *et al.*, 2007] and is particularly important for identifying local biospheric and volcanic influences on the baseline trace gas measurements (P. Tans and J. Miller, personal communication, 2009).

[34] The transition between the free troposphere and MBL air is a dominant feature in the measurement time series. The clusters of points along straight line sections in Figure 7b are associated with these transitions. Figure 13 shows the orbit of the mean diurnal cycle in q - $q\delta D$ phase space. The isotope ratio of the flux in the region of the transition between the MBL and the troposphere, δD_F , is found as the slope of the line. During the normal trade conditions, the mixing line as the MBL ascends (between 0900 and 1300 HAST) has $\delta D_F = -79.6 \pm 13.4\text{‰}$, which is statistically indistinguishable from the slope during the evening descent, which has $\delta D_F = -72.7 \pm 14.4\text{‰}$. (Uncertainty is quoted as 1 standard deviation error on the type-2 least squares fit accounting for both instrument measurement precision and the estimate of the mean of $n = 21$ days of normal trade conditions.) The regression with the ascending and descending components combined gives $\delta D_F = -76.6 \pm 9.9\text{‰}$ and is drawn in Figure 13.

[35] These values for δD_F are in the range of vapor in equilibrium with ocean water (values -70‰ to -83‰ for temperatures in the range 35°C – 20°C). When the MBL is saturated or near-saturated (say >0.8 h), the δD value remains close to the equilibrium value (consider relatively constant value of δD associated with the hyperbolic profile in Figure 5

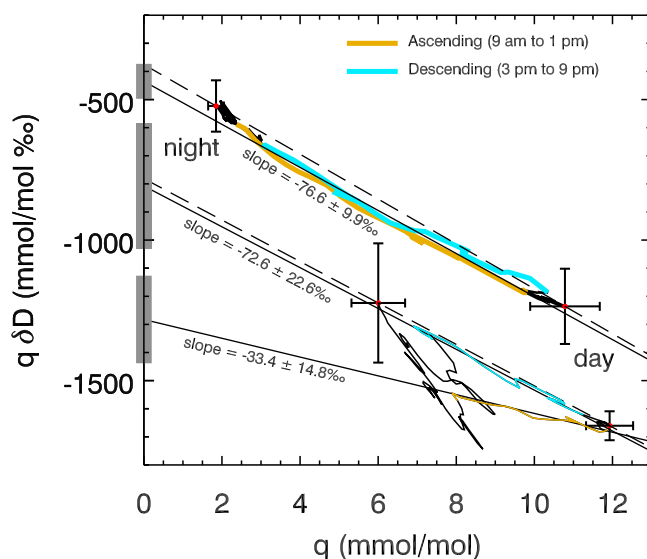


Figure 13. Mixing line analysis of the mean diurnal cycles shown in Figure 12. The thin curves are for the convective period between days 298 and 306, and the thick curves show the remainder of the record. The cyan section of curve shows data from the descending transition (1500–1900 HAST), and the orange curve shows data from the ascending transition (0900–1300 HAST), as indicated in Figure 12. The curves between the ascent and descent times are black. Red dots show the maximum and minimum values for q and the corresponding $q\delta D$ value. Dashed lines join the minimum and maximum points. Error bars at these points are the standard error for $N = 7$ for the moist period and $N = 21$ otherwise. Solid lines show the regression to the ascending and descending sections. Gray bars at $q = 0$ are the ± 1 standard deviation uncertainty on the regression intercept.

in the range $x = 0.8$ – 1). Under normal trade conditions, the MBL can be expected to be maintained near saturation and isotopic equilibrium since the time scale for evaporation at the atmosphere–ocean interface and turbulent mixing within the MBL is shorter than that of the exchange at the troposphere–MBL interface. Evaporation at the ocean–atmosphere interface is a disequilibrium process, and the value of δD_e is higher than the equilibrium value when the δD value of MBL is less than the equilibrium value. However, the newly evaporated water becomes homogenized with the preexisting vapor in the MBL by turbulent mixing, and it is this bulk water that is ultimately indicated by the δD_F values. Although evaporation is likely the dominant moistening processes, the role of other local influences such as sea spray or evapotranspiration cannot be ruled out in this analysis.

[36] During the convective period, the ascending and descending slopes are quite different: $-33.4 \pm 14.8\text{‰}$ during the ascent and $-72.62 \pm 22.6\text{‰}$ during the descent. The export of water from the region during the convective period is implied in Figure 13 as the displacement between the values at the end of the descent to the beginning of the ascent. This is seen in Figure 13 where the meandering (black) curve reconnects the cyan and orange curves near $q = 7$ mmol/mol. The variability in the shape of this curve reflects sampling over a small number of days. The relevant value for the ascent line is

sensitive to the exact time chosen as the termination of the transition and likely limited by the small number of days in the convective period (7 days). The δD_F during the descent is statistically indistinguishable from the case of the normal trade conditions and suggests that even during the convective period, the MBL becomes composed of vapor saturated with respect to the (nearby) ocean by the end of the day. During the ascent phase, however, the higher value of δD_F suggests a different mechanism. Figure 8b shows that the boundary layer relative humidity was lower ($\sim 60\%$) during this period. Following the *Craig and Gordon* [1965] evaporation model, lower humidity can give δD_e values of -30‰ with δD near the ocean surface approximately -100‰ and $\varepsilon_k = 5\text{‰}$. Therefore, during the convective period, the δD_F during ascent is consistent with a mechanism in which exchange between the troposphere and the MBL is enhanced and causes lower humidity and higher wind speed in the MBL, which enhances local evaporation. This result also suggests that the local evaporation contributes to the water balance of the moist filament rather than the filament being isolated from the surface.

[37] In the case of the normal trade conditions, the symmetry between the ascending and descending phases suggests almost complete reversibility and no net exchange of material across the MBL/troposphere interface. The mixing lines in this case simply describe a static spatial gradient. Figure 12 shows, however, that there is a moderate increase in the mean δD over the cycle of the MBL ascent and descent from δD from -263‰ at 0600 HAST to -246‰ at 2100 HAST, while q increases from 2.06 to 2.34 mmol/mol. This suggests that even during trade conditions, about 12% of the tropospheric water vapor observed at MLO is supplied in association with irreversible mixing at the MBL/troposphere interface. It is unclear if this is representative of the MBL or if it is a local effect associated with topography.

3.4. Characteristic Sources for Air Mass Mixing

[38] Figure 14 shows the joint probability distribution of all daytime (0900–1800 HAST) and nighttime (2100–0600 HAST) observations and plotted q – $q\delta D$. In an Eulerian framework, distinct air masses or mixing states are identified as those that are observed most frequently and produce local maxima in a probability distribution function [Plumb, 2002]. A number of distinct air masses can be identified in Figure 14. During the daytime, the MBL moisture is evident in both trade conditions and the convective period. A single dry air mass is evident during the trade conditions at around $q = 1$ mmol/mol. During the convective period, distinct fixed points are found between $q = 5$ and 11 mmol/mol. At nighttime, Figure 14d shows a local maximum at $q = 11$ mmol/mol, which is associated with the super-Rayleigh points identified in Figure 11.

[39] Periods of mixing are identified from each 1 h window of the time series as described in section 2.2. Recall from Figure 3 that air mass mixing can be identified in the time series data because the spatial gradients in the mixing zones pass by MLO on either diurnal or synoptic time scales. The mixing zone associated with fronts between two air masses moving in the horizontal expand from the tropics to the midlatitudes, and only a portion of the front is sampled at MLO, while the boundary layer mixing zone is local. Fifty-three percent of the time series is well explained by projecting

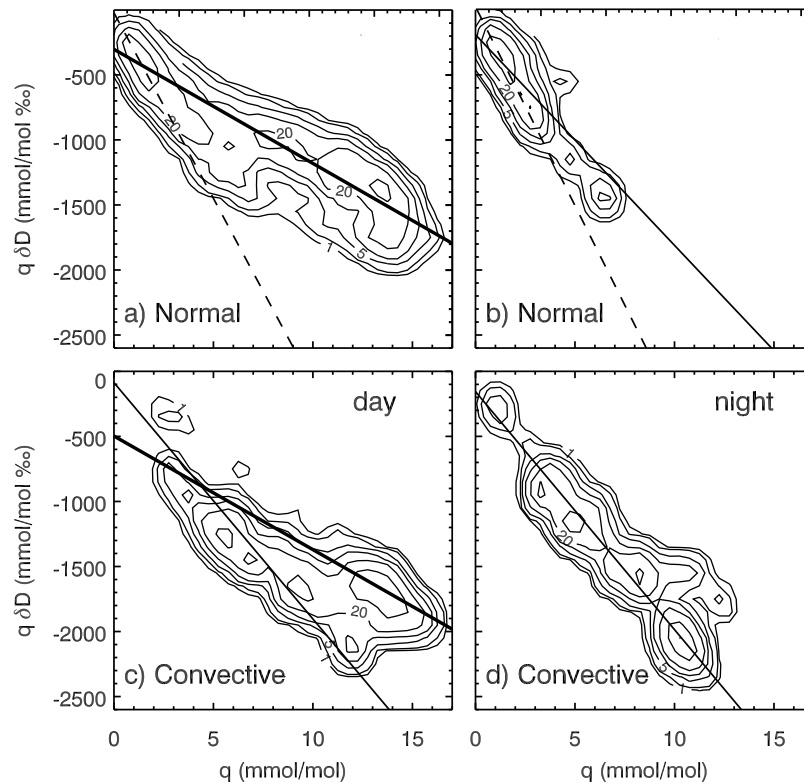


Figure 14. Joint probability distribution for (a and c) daytime (0900–1800 HAST) and (b and d) nighttime (2100–0600 HAST) observations. Figures 14a and 14b are associated with normal trade conditions, and Figures 14c and 14d are for the convective period. Probability distributions are constructed by binning data onto a grid of $\Delta(q\delta D) = 100\text{‰}$ and $\Delta q = 0.5 \text{ mmol/mol}$, smoothing with two applications of a weak filter on a 3×3 point stencil and normalizing to have a maximum value of 100. Contours are shown at 1, 2, 5, 10, 20, and 50. Mixing lines are plotted based on analysis in Figure 15. The bold line is associated with MBL transitions, the solid line is associated with a convective source, and the dashed line is associated with dry air.

the 1 hourly windowed data onto the (hyperbolic) mixing model (correlation squared between q and $q\delta D$ exceeding 0.8). This statistic is dominated by the mixing events that characterize the transition from day to night and night to day. Low correlation between δD and q (logarithmic, linear, or hyperbolic form) is found 31% of the time and identifies these times as periods in which the observations are within single distinct air masses (i.e., neither undergoing mixing nor condensation). Only 12% of the data can be explained as associated with a Rayleigh process (maximum correlation with logarithmic curve, rather than the hyperbolic mixing line), which is a reminder that the observations predominantly record the history of condensation rather than sampling an air mass that is actively condensing. The correlation analysis suggests that the subtropical water vapor distribution is best described as a sequence of distinct air masses that are continually being mixed.

[40] Figure 15 shows the probability distribution for δD_F values estimated from each 1 h window of the time series. Uncertainty is accounted for by constructing the probability distribution as the sum of the normal distributions described by the mean and standard deviation uncertainty on each δD_F estimate. The δD_F for daytime data for both the normal trade conditions and during the convective period shows the flux

associated with the MBL transition and the oceanic source. The mean values of δD_F are found by integrating the probability above -130‰ (note arrows in Figure 15 indicating local minima in the probability distribution) and are statistically indistinguishable from one another as found in the previous section (bold line in Figures 14a and 14c, which has $\delta D_F = -87.37\text{‰}$ and -87.30‰ , and uncertainty is given as the width of the feature in Figure 15). On the other hand, the nighttime data during trade conditions show two distinct sources: one with a peak near $\delta D_F = -161.9\text{‰}$ (Figure 14, dashed line) and one with a peak associated with $\delta D_F = -305.7\text{‰}$. The convective period has only a single clear flux value of $\delta D_F = -182.9\text{‰}$ at night (Figure 14, thin solid line). There is weak evidence that this source persists during the day $\delta D_F = -181.7\text{‰}$. From Figure 14 and recalling Figure 11, these values at night are associated with super-Rayleigh observations and other nighttime δD values consistent with a recent history of cloud processes. The lower δD_F values during the nighttime trade conditions are associated with low humidity air (Figure 14b).

[41] Given these fluxes, two distinct hydrological regimes for the nighttime (tropospheric) air observed are inferred. During the normal trade conditions, the MBL and the free topographic air are mostly isolated from one another, the

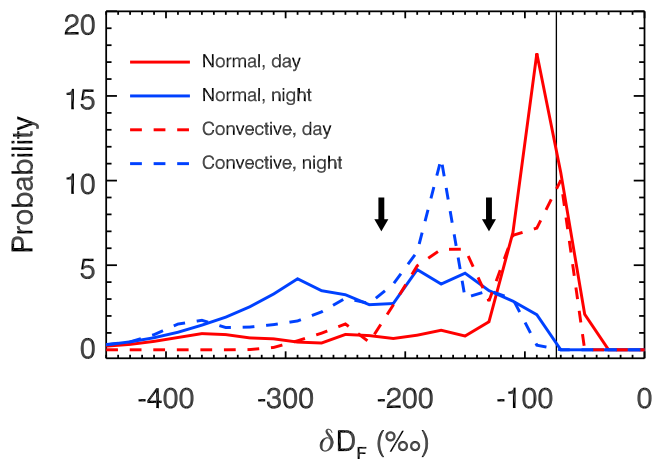


Figure 15. Probability distribution ($\times 1000$) of estimates of δD_F . Estimates are from each 1 h window of the time series in which the magnitude of correlation between $q\delta D$ and q exceeds 0.8 and also exceeds the correlation between δD and either q or $\ln(q)$. The distribution function takes into account the uncertainty in the individual δD_F estimates. Arrows are shown at $\delta D_F = -130\text{‰}$ and -220‰ , which are chosen as the division between distinct features in the distribution. The curves correspond to each of the distributions in Figure 14. Normal trade conditions are shown as solid curves, and the convective period (days 298–306) shown as dashed curves. Values for daytime are red, and values for nighttime are blue as in Figure 14. The vertical line at $\delta D = -73.7\text{‰}$ is for vapor in equilibrium with seawater at 25°C .

water balance is associated with a supply of high δD air by cumulous clouds (specifically, detrainment of total water), and the dehydration that results from irreversible mixing with dry air of latitude or high-altitude origin. During convective periods, the principal balance is between the supply of boundary layer vapor during the day and export of water by the large-scale advection that is associated with high humidity and convective cloud.

4. Discussion

[42] The boundary layer diurnal cycle is a known topographically forced feature observed at MLO [Cao *et al.*, 2007], and the mixing processes that were observed may not be representative of the regional MBL. The twice-daily radiosonde analysis showed, for instance, that the MBL displays little variability when the balloon is downstream from the launch and presumably over the ocean. The isotope ratio data show that while the mixing signal dominates, the average daytime data do not fall on a mixing line with an oceanic source and therefore there is also a signature of the history of condensation within the MBL. The importance of clouds in the boundary layer has been recognized in other studies in oceanic areas [e.g., Albrecht, 1989; Larson *et al.*, 1999; Osborne *et al.*, 2000; Teixeira *et al.*, 2008; Fletcher and Bretherton, 2010]. It is found that the boundary layer isotopic moisture balance during trade conditions is quite different from that observed in regions of deep convection, where shallow cumuli seemingly play a smaller role relative to the drying by downdrafts. It is apparent, however, that

constraining the MBL water balance with isotopic information is ultimately hindered by the lack of vertical profile measurements.

[43] Measurements from MLO are qualitatively consistent with a mechanism in which the humidity is set upstream by condensation and advected into the region, and the time-mean humidity is treated as the ensemble of isolated parcels. The driest air over Hawaii during the study period is linked to anticyclonic intrusions from higher latitudes. However, the isotopic composition of this air is not consistent with the prediction from a Rayleigh model. Because the dew point temperature was significantly below freezing, ice would have formed and justifies the choice of a Rayleigh model for some fraction of parcels; however, the role of free air mixing, precipitation efficiency, and supersaturation also appears important since they are required to fully explain the non-Rayleigh nighttime mean values observed. The dry and lowest δD values at MLO that originate from the north are qualitatively consistent with predictions from simple Eulerian advection modeling studies [Galewsky and Hurley, 2010]. However, mixing processes like those identified here cause isotope ratios that are non-Rayleigh even if the two air masses are set via Rayleigh processes. Therefore, the deviation from a Rayleigh prediction provides new insight into the strength of air mass mixing between filamentary structures in the troposphere. Furthermore, the deviation of isotopic measurements from model simulations that account for only advection and (Rayleigh) condensation provide information specific to the types of cloud microphysics occurring upstream. In particular, the amount of detrainment and precipitation efficiency are critical parameters in setting the mean humidity of the troposphere in climate models [Bony and Emanuel, 2005], and they are both identified (qualitatively) here by the mismatch of the data with Rayleigh models. Given better constraint on the isotopic history along the trajectories, the results suggest that estimates of the precipitation efficiency should be attainable.

[44] It is clear that filaments that transport moisture meridionally play an important role in the subtropical water balance [Pierrehumbert and Yang, 1993]. The time-mean humidity depends on the frequency of moist plumes (we observed one). The measurements show the isotopic conditions of moist plumes near their subtropical origin and complement the precipitation-based studies of systems that make landfall on the North American coast [Coplen *et al.*, 2008; Yoshimura *et al.*, 2010]. The δD_F derived from MLO observations provides new insight into transport processes because it identifies the source water independently of the water mixing ratio. The values found during the convective period raise the possibility of deducing what fraction of water that arrives at higher latitudes is associated with a purely equatorial origin versus water that is entrained into the filament in association with local evaporation during poleward transit. While the mixing analysis suggests that the convective period has a considerable contribution from local (MBL) sources, a complete analysis will require an adequate set of atmospheric vapor measurements at higher-latitude regions to compare with values in the equatorial origin of the moisture. This study shows that a detailed description of the subtropical moisture budget is fundamentally incomplete without both accounting for the climatology of the moist plumes from the deep tropics and achieving a deeper under-

standing of the roles that cloud microphysical exchanges and cloud macrophysical organization have on moistening of the subtropics.

5. Conclusions

[45] Mauna Loa measurements of the isotopic composition of water vapor show the influences of synoptic scale variability in the free troposphere at night and the influences of MBL air during the day. After careful calibration for the absolute scale, and by applying a correction for humidity dependence, continuous spectroscopic isotopic analyzers provide robust measurements that enable unprecedented insight into the hydrology of the atmosphere using isotopic methods. The diurnal and synoptic scale variability is large (order of 100‰). The analysis suggests that the subtropical tropospheric water vapor distribution is well described as mixing between distinct air masses, with the joint q - δD state of the air masses set by the condensation and evaporation history upstream. From counting statistics, 31% of air is distinct and not undergoing mixing, while 53% of the atmosphere sampled by time is associated with mixing. The station observations capture this mixing because advection moves the mixing zones across MLO both vertically during MBL transitions and at night in association with mostly horizontal transport in the free troposphere. While the mixing analysis is a powerful tool in extracting unique information from paired measurements of δD and q , there is a need for better isotopic information (observations or models) about candidate sources to fully interpret the δD_F value. Nonetheless, the finding that mixing gradients (in space and time) are a prevalent characteristic of the atmospheric water vapor field begins to advance descriptions of atmospheric humidity beyond considering parcels in isolation.

[46] One objective of this study was to confirm that modern instruments are able to measure isotopic composition with sufficient fidelity to identify salient features of the subtropical tropospheric humidity and the processes that contribute to its mean state. We have established that the instruments can robustly capture the meteorologically relevant variability and can provide insight into the history of cloud and mixing processes. The results provide insight into the balances between large-scale (mostly lateral) advective processes, cloud detrainment, and boundary layer processes. Because of the relatively short (4 week) duration of the experiment, climatological conclusions cannot be drawn, but many of the processes that contribute to the long-term mean state were observed. Moreover, one might expect the results to depend on season (for instance, moist filaments are rare during summer) and thereby offer an opportunity to track seasonal moisture sources by the changing balances of processes expressed in the isotope ratios.

[47] The success of this study provides assurance that a continued water isotopologue monitoring program would provide useful statistics on the processes that contribute to the regional moisture balance. Recent modeling and studies of gridded meteorological analyses have shown that the mean overturning circulation and the humidity of the subtropics are changing [Held and Soden, 2006; Seidel et al., 2008; Laliberté and Pauluis, 2010]. These changes are synonymous with a shift in the population of distinct air masses and the statistical characteristics of mixing that describe the time

mean state. Records of the isotopic composition from Mauna Loa and other free tropospheric observatories may thus become particularly valuable for observing subtle hydrological responses to global climate variability and change.

[48] **Acknowledgments.** This work was supported by the National Science Foundation Climate and Large-scale Dynamics program under grants 0840129 and 0840168 to D.N., J.G., and Z.D.S. and by the NASA Jet Propulsion Laboratory. We thank all the staff at Mauna Loa Observatory and the NOAA office in Hilo who helped with logistics and daily operations during the field campaign. Isotope ratio data from this study are available in raw and calibrated form from <http://climate.colorado.edu/research/HAWAII>.

References

- Albrecht, B. A. (1989), Aerosols, cloud microphysics, and fractional cloudiness, *Science*, 245(4923), 1227–1230, doi:10.1126/science.245.4923.1227.
- Arrhenius, S. (1896), On the influence of carbonic acid in the air upon the temperature of the ground, *London, Edinburgh, and Dublin Philos. Mag. J. Sci.*, 41, 690–705.
- Bigeleisen, J. (1961), Statistical mechanics of isotope effects on the thermodynamic properties of condensed systems, *J. Chem. Phys.*, 34, 1485–1493, doi:10.1063/1.1701033.
- Bony, S., and K. A. Emanuel (2005), On the role of moist processes in tropical intraseasonal variability: Cloud-radiation and moisture-convection feedbacks, *J. Atmos. Sci.*, 62(8), 2770–2789, doi:10.1175/JAS3506.1.
- Bony, S., et al. (2006), How well do we understand and evaluate climate change feedback processes?, *J. Clim.*, 19(15), 3445–3482, doi:10.1175/JCLI3819.1.
- Bretherton, C. S., P. Austin, and S. T. Siems (1995), Cloudiness and marine boundary-layer dynamics in the Astex Lagrangian experiments. Part 2. Cloudiness, drizzle, surface fluxes, and entrainment, *J. Atmos. Sci.*, 52(16), 2724–2735, doi:10.1175/1520-0469(1995)052<2724:CAMBLD>2.0.CO;2.
- Cao, G. X., T. W. Giambelluca, D. E. Stevens, and T. A. Schroeder (2007), Inversion variability in the Hawaiian trade wind regime, *J. Clim.*, 20(7), 1145–1160, doi:10.1175/JCLI4033.1.
- Cau, P., J. Methven, and B. Hoskins (2007), Origins of dry air in the tropics and subtropics, *J. Clim.*, 20(12), 2745–2759, doi:10.1175/JCLI4176.1.
- Chen, Y. L., and J. H. Feng (2001), Numerical simulations of airflow and cloud distributions over the windward side of the island of Hawaii. Part I: The effects of trade wind inversion, *Mon. Weather Rev.*, 129(5), 1117–1134, doi:10.1175/1520-0493(2001)129<1117:NSOAC>2.0.CO;2.
- Coplen, T. B. (1995), Discontinuity of SMOW and PDB, *Nature*, 375(6529), 285, doi:10.1038/375285a0.
- Coplen, T. B., P. J. Neiman, A. B. White, J. M. Landwehr, F. M. Ralph, and M. D. Dettinger (2008), Extreme changes in stable hydrogen isotopes and precipitation characteristics in a landfalling Pacific storm, *Geophys. Res. Lett.*, 35, L21808, doi:10.1029/2008GL035481.
- Couhert, A., T. Schneider, J. L. Li, D. E. Waliser, and A. M. Tompkins (2010), The maintenance of the relative humidity of the subtropical free troposphere, *J. Clim.*, 23(2), 390–403, doi:10.1175/2009JCLI2952.1.
- Craig, H., and L. I. Gordon (1965), Deuterium and oxygen-18 variations in the ocean and marine atmosphere, in *Proceedings of Conference on Stable Isotopes in Oceanic Studies and Paleotemperatures*, edited by E. Tongiorgi, pp. 9–130, Lab. Geol. and Nuclear Sci., Spoleto, Italy.
- Dansgaard, W. (1953), The abundance of O^{18} in atmospheric water and water vapour, *Tellus*, 5, 461–469, doi:10.1111/j.2153-3490.1953.tb01076.x.
- Ehhalt, D. H. (1974), Vertical profiles of HTO, HDO and H_2O in the troposphere, *Rep. NCAR-TN/STR-100*, Natl. Cent. for Atmos. Res., Boulder, Colo.
- Ehhalt, D. H., F. Rohrer, and A. Fried (2005), Vertical profiles of HDO/ H_2O in the troposphere, *J. Geophys. Res.*, 110, D13301, doi:10.1029/2004JD005569.
- Fletcher, J. K., and C. S. Bretherton (2010), Evaluating boundary layer-based mass flux closures using cloud-resolving model simulations of deep convection, *J. Atmos. Sci.*, 67(7), 2212–2225, doi:10.1175/2010JAS3328.1.
- Frankenberg, C., et al. (2009), Dynamic processes governing lower-tropospheric HDO/ H_2O ratios as observed from space and ground, *Science*, 325(5946), 1374–1377, doi:10.1126/science.1173791.
- Galewsky, J., and J. V. Hurlley (2010), An advection-condensation model for subtropical water vapor isotopic ratios, *J. Geophys. Res.*, 115, D16116, doi:10.1029/2009JD013651.

- Galewsky, J., A. Sobel, and I. Held (2005), Diagnosis of subtropical humidity dynamics using tracers of last saturation, *J. Atmos. Sci.*, 62(9), 3353–3367, doi:10.1175/JAS3533.1.
- Gat, J. R. (1996), Oxygen and hydrogen isotopes in the hydrologic cycle, *Annu. Rev. Earth Planet. Sci.*, 24, 225–262, doi:10.1146/annurev.earth.24.1.225.
- Gat, J. R. (2000), Atmospheric water balance—The isotopic perspective, *Hydrol. Processes*, 14(8), 1357–1369, doi:10.1002/1099-1085(20000615)14:8<1357::AID-HYP986>3.0.CO;2-7.
- Goldman, M. A. (1974), Carbon dioxide measurements and local wind patterns at Mauna Loa Observatory, Hawaii, *J. Geophys. Res.*, 79(30), 4550–4554, doi:10.1029/JC079i030p04550.
- Gupta, P., D. Noone, J. Galewsky, C. Sweeney, and B. H. Vaughn (2009), Demonstration of high-precision continuous measurements of water vapor isotopologues in laboratory and remote field deployments using wavelength-scanned cavity ring-down spectroscopy (WS-CRDS) technology, *Rapid Commun. Mass Spectrom.*, 23(16), 2534–2542, doi:10.1002/rcm.4100.
- He, H., and R. B. Smith (1999), Stable isotope composition of water vapor in the atmospheric boundary layer above the forests of New England, *J. Geophys. Res.*, 104, 11,657–11,673, doi:10.1029/1999JD900080.
- Held, I. M., and B. J. Soden (2006), Robust responses of the hydrological cycle to global warming, *J. Clim.*, 19(21), 5686–5699, doi:10.1175/JCLI3990.1.
- Herbin, H., D. Hurtmans, C. Clerbaux, L. Clarisse, and P.-F. Coheur (2009), H₂¹⁶O and HDO measurements with IASI/MetOp, *Atmos. Chem. Phys. Disc.*, 9, 9267–9290, doi:10.5194/acpd-9-9267-2009.
- Hurley, J. V., and J. Galewsky (2010), A last-saturation diagnosis of subtropical water vapor response to global warming, *Geophys. Res. Lett.*, 37, L06702, doi:10.1029/2009GL042316.
- Iannone, R. Q., D. Romanini, O. Cattani, H. A. J. Meijer, and E. R. T. Kerstel (2010), Water isotope ratio ($\delta^2\text{H}$ and $\delta^{18}\text{O}$) measurements in atmospheric moisture using an optical feedback cavity enhanced absorption laser spectrometer, *J. Geophys. Res.*, 115, D10111, doi:10.1029/2009JD012895.
- Johnson, L. R., Z. D. Sharp, J. Galewsky, M. Strong, A. van Pelt, and D. Noone (2011), Laser instrument measurement bias at low water vapor concentrations: Applications to measurements from Mauna Loa Observatory, Hawaii, *Rapid Commun. Mass Spectrom.*, 25(5), 608–616, doi:10.1002/rcm.4894.
- Jouzel, J. (1986), Isotopes in cloud physics: Multistep and multistage processes, in *Handbook of Environmental Isotope Geochemistry*, vol. 2, *The Terrestrial Environment B*, edited by P. Fritz and J. C. Fontes, pp. 61–112, Elsevier, New York.
- Kalnay, E., et al. (1996), The NCEP/NCAR 40-year reanalysis project, *Bull. Am. Meteorol. Soc.*, 77, 437–471, doi:10.1175/1520-0477(1996)077<0437:TNYRP>2.0.CO;2.
- Keeling, C. D. (1958), The concentration and isotopic abundances of atmospheric carbon dioxide in rural areas, *Geochim. Cosmochim. Acta*, 13(4), 322–334, doi:10.1016/0016-7037(58)90033-4.
- Kerstel, E. R. T., R. Q. Iannone, M. Chenevier, S. Kassj, H. J. Jost, and D. Romanini (2006), A water isotope (^2H , ^{17}O , and ^{18}O) spectrometer based on optical feedback cavity-enhanced absorption for in situ airborne applications, *Appl. Phys. B*, 85(2–3), 397–406, doi:10.1007/s00340-006-2356-1.
- Laliberté, F., and O. Pauluis (2010), Winter intensification of the moist branch of the circulation in simulations of 21st century climate, *Geophys. Res. Lett.*, 37, L20707, doi:10.1029/2010GL045007.
- Larson, K., D. L. Hartmann, and S. A. Klein (1999), The role of clouds, water vapor, circulation, and boundary layer structure in the sensitivity of the tropical climate, *J. Clim.*, 12(8), 2359–2374, doi:10.1175/1520-0442(1999)012<2359:TROCWV>2.0.CO;2.
- Lis, G., L. I. Wassenaar, and M. J. Hendry (2008), High-precision laser spectroscopy D/H and $^{18}\text{O}/^{16}\text{O}$ measurements of microliter natural water samples, *Anal. Chem.*, 80(1), 287–293, doi:10.1021/ac701716q.
- Manabe, S., and R. T. Wetherald (1975), Effects of doubling CO₂ concentration on climate of a general circulation model, *J. Atmos. Sci.*, 32(1), 3–15, doi:10.1175/1520-0469(1975)032<0003:TEODTC>2.0.CO;2.
- McGuirk, J. P., and D. J. Ulsh (1990), Evolution of tropical plumes in water-vapor imagery, *Mon. Weather Rev.*, 118(9), 1758–1766, doi:10.1175/1520-0493(1990)118<1758:EOTPIV>2.0.CO;2.
- Medeiros, B., A. Hall, and B. Stevens (2005), What controls the mean depth of the PBL?, *J. Clim.*, 18(16), 3157–3172, doi:10.1175/JCLI3417.1.
- Merlivat, L., and J. Jouzel (1979), Global climatic interpretation of the deuterium-oxygen 18 relationship for precipitation, *J. Geophys. Res.*, 84, 5029–5033, doi:10.1029/JC084iC08p05029.
- Miller, J. B., and P. P. Tans (2003), Calculating isotopic fractionation from atmospheric measurements at various scales, *Tellus, Ser. B*, 55(2), 207–214, doi:10.1034/j.1600-0889.2003.00020.x.
- Minschwaner, K., and A. E. Dessler (2004), Water vapor feedback in the tropical upper troposphere: Model results and observations, *J. Clim.*, 17(6), 1272–1282, doi:10.1175/1520-0442(2004)017<1272:WVFITT>2.0.CO;2.
- Morrison, I., and S. Businger (2001), Synoptic structure and evolution of a Kona Low, *Weather Forecasting*, 16(1), 81–98, doi:10.1175/1520-0434(2001)016<0081:SSAEOA>2.0.CO;2.
- Newell, R. E., N. E. Newell, Y. Zhu, and C. Scott (1992), Tropospheric rivers?—A pilot study, *Geophys. Res. Lett.*, 19(24), 2401–2404, doi:10.1029/92GL02916.
- Noone, D., and I. Simmonds (1999), A three-dimensional spherical trajectory algorithm, in *Research Activities in Atmospheric and Oceanic Modelling*, edited by H. Ritchie, Rep. 28, WMO/TD-No. 942, pp. 943.926–943.927, World Meteorol. Organ., Geneva, Switzerland.
- Noone, D., J. Turner, and R. Mulvaney (1999), Atmospheric signals and characteristics of accumulation in Dronning Maud Land, Antarctica, *J. Geophys. Res.*, 104, 19,191–19,211, doi:10.1029/1999JD900376.
- Osborne, S. R., et al. (2000), Evolution of the aerosol, cloud and boundary-layer dynamic and thermodynamic characteristics during the 2nd Lagrangian experiment of ACE-2, *Tellus, Ser. B*, 52(2), 375–400, doi:10.1034/j.1600-0889.2000.00051.x.
- Payne, V. H., D. Noone, A. Dudhia, C. Piccolo, and R. G. Grainger (2007), Global satellite measurements of HDO and implications for understanding the transport of water vapour into the stratosphere, *Q. J. R. Meteorol. Soc.*, 133(627), 1459–1471, doi:10.1002/qj.127.
- Pierrehumbert, R. T. (1995), Thermostats, radiator fins, and the local runaway greenhouse, *J. Atmos. Sci.*, 52(10), 1784–1806, doi:10.1175/1520-0469(1995)052<1784:TRFATL>2.0.CO;2.
- Pierrehumbert, R. T., and R. Roca (1998), Evidence for control of Atlantic subtropical humidity by large scale advection, *Geophys. Res. Lett.*, 25(24), 4537–4540, doi:10.1029/1998GL900203.
- Pierrehumbert, R. T., and H. Yang (1993), Global chaotic mixing on isentropic surfaces, *J. Atmos. Sci.*, 50(15), 2462–2480, doi:10.1175/1520-0469(1993)050<2462:GCMOIS>2.0.CO;2.
- Pierrehumbert, R. T., H. Brogniez, and R. Roca (2007), On the relative humidity of Earth's atmosphere, in *The Global Circulation of the Atmosphere: Phenomena, Theory, Challenges*, edited by T. Schneider and A. H. Sobel, pp. 143–185, Princeton Univ. Press, Princeton, N. J.
- Plumb, R. A. (2002), Stratospheric transport, *J. Meteorol. Soc. Jpn.*, 80(4B), 793–809, doi:10.2151/jmsj.80.793.
- Rozanski, K., and C. Sonntag (1982), Vertical distribution of deuterium in atmospheric water vapour, *Tellus*, 34, 135–141, doi:10.1111/j.2153-3490.1982.tb01800.x.
- Ryoo, J. M., T. Igusa, and D. W. Waugh (2009), PDFs of tropical tropospheric humidity: Measurements and theory, *J. Clim.*, 22(12), 3357–3373, doi:10.1175/2008JCLI2747.1.
- Salathé, E. P., and D. L. Hartmann (1997), A trajectory analysis of tropical upper-tropospheric moisture and convection, *J. Clim.*, 10(10), 2533–2547, doi:10.1175/1520-0442(1997)010<2533:ATAOTU>2.0.CO;2.
- Sayres, D. S., L. Pfister, T. F. Hanisco, E. J. Moyer, J. B. Smith, J. M. St. Clair, A. S. O'Brien, M. F. Witinski, M. Legg, and J. G. Anderson (2010), Influence of convection on the water isotopic composition of the tropical tropopause layer and tropical stratosphere, *J. Geophys. Res.*, 115, D00J20, doi:10.1029/2009JD013100.
- Schmidt, G. A., R. A. Ruedy, R. L. Miller, and A. A. Lacis (2010), Attribution of the present-day total greenhouse effect, *J. Geophys. Res.*, 115, D20106, doi:10.1029/2010JD014287.
- Schneider, M., K. Yoshimura, F. Hase, and T. Blumenstock (2010a), The ground-based FTIR network's potential for investigating the atmospheric water cycle, *Atmos. Chem. Phys.*, 10(7), 3427–3442, doi:10.5194/acp-10-3427-2010.
- Schneider, T., P. A. O'Gorman, and X. J. Levine (2010b), Water vapor and the dynamics of climate changes, *Rev. Geophys.*, 48, RG3001, doi:10.1029/2009RG000302.
- Seidel, D. J., Q. Fu, W. J. Randel, and T. J. Reichler (2008), Widening of the tropical belt in a changing climate, *Nat. Geosci.*, 1(1), 21–24.
- Sherwood, S. C. (1996a), Maintenance of the free-tropospheric tropical water vapor distribution. Part 1. Clear regime budget, *J. Clim.*, 9(11), 2903–2918, doi:10.1175/1520-0442(1996)009<2903:MOTFTT>2.0.CO;2.
- Sherwood, S. C. (1996b), Maintenance of the free-tropospheric tropical water vapor distribution. Part 2. Simulation by large-scale advection, *J. Clim.*, 9(11), 2919–2934, doi:10.1175/1520-0442(1996)009<2919:MOTFTT>2.0.CO;2.

- Sherwood, S. C., R. Roca, T. M. Weckwerth, and N. G. Andronova (2010), Tropospheric water vapor, convection, and climate, *Rev. Geophys.*, **48**, RG2001, doi:10.1029/2009RG000301.
- Strong, M., Z. D. Sharp, and D. S. Gutzler (2007), Diagnosing moisture transport using D/H ratios of water vapor, *Geophys. Res. Lett.*, **34**, L03404, doi:10.1029/2006GL028307.
- Teixeira, J., P. May, M. Flatau, and T. F. Hogan (2008), SST sensitivity of a global ocean-atmosphere coupled system to the parameterization of boundary layer clouds, *J. Mar. Syst.*, **69**(1–2), 29–36, doi:10.1016/j.jmarsys.2007.02.012.
- Weber, R. J., and P. H. McMurry (1996), Fine particle size distributions at the Mauna Loa Observatory, Hawaii, *J. Geophys. Res.*, **101**(D9), 14,767–14,775, doi:10.1029/95JD02271.
- Webster, C. R., and A. J. Heymsfield (2003), Water isotope ratios D/H, $^{18}\text{O}/^{16}\text{O}$, $^{17}\text{O}/^{16}\text{O}$ in and out of clouds map dehydration pathways, *Science*, **302**(5651), 1742–1745, doi:10.1126/science.1089496.
- Worden, J., et al. (2006), Tropospheric emission spectrometer observations of the tropospheric HDO/H₂O ratio: Estimation approach and characterization, *J. Geophys. Res.*, **111**, D16309, doi:10.1029/2005JD006606.
- Worden, J., D. Noone, and K. Bowman (2007), Importance of rain evaporation and continental convection in the tropical water cycle, *Nature*, **445**(7127), 528–532, doi:10.1038/nature05508.
- Yoshimura, K., M. Kanamitsu, and M. Dettinger (2010), Regional down-scaling for stable water isotopes: A case study of an atmospheric river event, *J. Geophys. Res.*, **115**, D18114, doi:10.1029/2010JD014032.
- Zhu, Y., and R. E. Newell (1994), Atmospheric rivers and bombs, *Geophys. Res. Lett.*, **21**(18), 1999–2002, doi:10.1029/94GL01710.
- D. Baer and F. Dong, Los Gatos Research, Inc., 67 E. Evelyn Ave., Ste. 3, Mountain View, CA 94041-1529, USA.
- A. Bailey, D. P. Brown, D. Noone, and D. Toohey, Department of Atmospheric and Oceanic Sciences, University of Colorado at Boulder, Campus Box 216, Boulder, CO 80309-0216, USA. (dcn@colorado.edu)
- J. Barnes, Mauna Loa Observatory, National Atmospheric and Oceanic Administration, 1437 Kilauea Ave., Hilo, HI 96720, USA.
- L. Christensen and J. Worden, Jet Propulsion Laboratory, California Institute of Technology, 4800 Oak Grove Dr., Pasadena, CA 91109, USA.
- E. Crosson and A. Van Pelt, Picarro, Inc., 3105 Patrick Henry Dr., Santa Clara, CA 95054, USA.
- J. Galewsky, J. V. Hurley, L. R. Johnson, Z. D. Sharp, and M. Strong, Department of Earth and Planetary Sciences, University of New Mexico, MSC 03 2040, Albuquerque, NM 87131, USA.
- J. S. Wright, Department of Applied Mathematics and Theoretical Physics, University of Cambridge, Wilberforce Road, Cambridge CB4 1EN, UK.